

Elucidation of opto-electronic and photoelectrochemical properties of FeVO₄ photoanodes for solar water oxidation

Mengyuan Zhang,^{a,b} Yimeng Ma,^b Dennis Friedrich,^b Roel van de Krol,^{b,c} Lydia H. Wong^{*a} and Fatwa F. Abdi^{*b}

Received 00th January 20xx,
Accepted 00th January 20xx

DOI: 10.1039/x0xx00000x

www.rsc.org/

Triclinic iron vanadate (n-type FeVO₄) thin films were fabricated for the first time by spray pyrolysis and elucidated as a potential photoanode material for solar water oxidation. FeVO₄ has an ideal band gap for a photoanode of ~2.0 eV, which corresponds to a potential solar-to-hydrogen (STH) efficiency of 16%. However, our findings show that the photoelectrochemical performance of FeVO₄ is limited by very poor charge carrier separation efficiency in the bulk. Time-resolved microwave conductivity (TRMC) measurements revealed that the low mobility (~5×10⁻⁵ cm² V⁻¹ s⁻¹) and short diffusion length (~2 nm) of undoped FeVO₄ are the main reason for its fast bulk recombination. To overcome the poor charge separation efficiency in the bulk, molybdenum doping was used to enhance its mobility, lifetime, and carrier concentration. Doping with 2% Mo increased the photocurrent density by more than 45% at 1.6 V vs. RHE. Finally, we show that the near-ideal band gap of FeVO₄ can be combined with the favorable carrier mobility of BiVO₄ in a mixed phase compound, Fe_{1-x}Bi_xVO₄, a new photoanode candidate for solar water splitting.

Introduction

The successful development of bismuth vanadate (BiVO₄) as a photoanode for solar water splitting has generated increasing interest on complex metal oxides. Despite common limitations of modest surface catalytic activity, poor carrier transport and moderate optical absorption,¹⁻³ various methods can be implemented to solve these problems. In the case of BiVO₄, for example, surface modification layers,^{4, 5} doping,⁶⁻¹¹ and nanostructuring^{1, 12-14} have been successfully used to achieve impressive performance enhancements. The combination of these has led to the highest reported photocurrent density of 6.72 mA cm⁻² from a BiVO₄-based nanostructured photoanode, which corresponds to 90% of the theoretical maximum photocurrent density based on its band gap of 2.4 eV (7.5 mA cm⁻²).¹⁵ While this record photocurrent density is encouraging, it also serves as a reminder that the performance of BiVO₄ photoanodes is intrinsically limited by its relatively large band gap (2.4 eV).¹⁶ In order to further enhance the efficiency, a complex metal oxide with a band gap smaller than that of BiVO₄ is therefore desired. Calculations have shown that a photoanode with a band gap of ~1.7-1.9 eV can potentially result in STH efficiency higher than 20% when combined with

~1.0-1.3 eV bottom absorber in a tandem configuration.¹⁷⁻²⁰ Several promising candidates are available for a small band gap photocathode (e.g., Si, WSe₂, InP),²¹⁻²⁴ but a good candidate for a photoanode with a band gap of 1.7–1.9 eV is, unfortunately, still not obvious.

To solve the above limitations, researchers have turned their attention to many novel or less investigated semiconductors.^{2, 3} Among these, iron (III) vanadate (FeVO₄) is one possible candidate. This n-type semiconductor has a triclinic crystal structure consisting of [FeO₆] octahedrons and [FeO₅] distorted trigonal bipyramids, with [VO₄] tetrahedrons connecting the two structures.²⁵ It was first identified by a high-throughput screening method as a potential photoelectrode material with good absorption in the visible part of the solar spectrum.²⁶ The band gap of FeVO₄ is reported to be ~2.0-2.1 eV;²⁷⁻²⁹ while it is slightly larger than the ideal 1.7-1.9 eV, the theoretical achievable STH efficiency is still a respectable 16%. The photocurrent density of the undoped material is, however, less than 0.1 mA cm⁻² at 1.23 V vs. RHE (potential relative to reversible hydrogen electrode).²⁷ Efforts have been reported to improve the performance (e.g., doping with W, partial reduction of Fe³⁺/Fe²⁺),^{28, 30} but the photocurrent enhancement has been marginal. The cause of such a small photocurrent is not clear, because many intrinsic properties, such as the exact band positions, carrier mobility, and carrier lifetime are still unknown. Elucidation of these properties will allow us to identify the performance limiting factors and apply appropriate improvement strategies.

In this work, we employed spray pyrolysis to fabricate crystalline thin film FeVO₄ photoanodes. After heat treatment at 650 °C to obtain the desired phase, the film was subjected to a combination of photoelectrochemical and time-resolved

^a School of Materials Science and Engineering, Nanyang Technological University, Nanyang Avenue, Singapore 639798. Email: lydiawong@ntu.edu.sg

^b Institute for Solar Fuels, Helmholtz-Zentrum Berlin für Materialien und Energie GmbH, Hahn-Meitner-Platz 1, Berlin 14109, Germany. Email: fatwa.abdi@helmholtz-berlin.de

^c Institut für Chemie, Technische Universität Berlin, Straße des 17. Juni 124, 10623 Berlin, Germany.

Electronic Supplementary Information (ESI) available: [details of any supplementary information available should be included here]. See DOI: 10.1039/x0xx00000x

microwave conductivity (TRMC) measurements. The photocurrent of FeVO₄ was found to be limited by poor charge separation efficiency, caused by a very low carrier mobility. Based on this insight, we introduced molybdenum (Mo) as dopant and successfully improved the carrier transport properties as well as photoelectrochemical performance. We conclude by exploring a mixture of FeVO₄ and BiVO₄ (i.e., Fe_{1-x}Bi_xVO₄) in order to further improve the photoelectrochemical performance.

Experimental

Sample fabrication

The FeVO₄ films were fabricated using a simple spray pyrolysis method. The details of the spray setup and deposition process can be found in previous reports.^{6,31} The precursor solution was prepared by dissolving 20 mM Fe(C₅H₇O₂)₃ (99.9%, Sigma Aldrich) and 20 mM VO(C₅H₇O₂)₂ (99%, Acros Organics) in absolute ethanol (Sigma Aldrich). For Mo doped samples, MoO₂(C₅H₇O₂)₂ (Sigma Aldrich) was added into the precursor while keeping the molar ratio Fe/(V+Mo) = 1. The volume of precursor was adjusted according to the thickness of film to be deposited (e.g., 25 mL precursor for ~100 nm film). FTO substrates (TEC-7, Pilkington) were placed on the hot plate, which was heated to 450 °C before deposition. The spray rate was controlled to be ~1.5 mL/cycle, with each cycle containing 5 s spray time and 55 s rest time. The rest time was necessary to allow complete evaporation of the solvent and pyrolysis of acetylacetonate ligands. As-deposited films were then annealed at 650 °C for 2 min in technical air (20% O₂, 80% N₂) with a ramp rate of 15 °C/min. For time-resolved microwave conductivity measurements, the films were deposited on quartz substrates (2.5 × 1.2 cm², Spectrosil 2000, Heraeus) using the same spray procedure.

Characterizations

X-ray diffraction measurements were performed using a Bruker D8 Advance X-ray diffractometer (Cu-Kα, λ = 0.154056 nm) in a grazing incidence configuration with an incidence angle of 0.5°. Scanning electron micrographs (SEM) were taken with a LEO GEMINI scanning electron microscope at an accelerating voltage of 5 kV. UV-vis absorption spectra were measured in an integrating sphere using a PerkinElmer Lambda 950 spectrometer. Elemental analysis using X-ray photoelectron spectroscopy (XPS) was carried out with a monochromatic Al Kα X-ray source (1486.74 eV, Specs Focus 500 monochromator) and a hemispherical analyzer (Specs Phoibos 100) in an ultrahigh vacuum system (base pressure ~10⁻⁸ mbar). Ultraviolet photoelectron spectroscopy (UPS) was conducted using He I source (E = 21.218 eV) with the same hemispherical analyzer as in the XPS measurement. Atomic force microscopy (Park Systems XE70) was used to measure the surface roughness of the films.

Time-resolved microwave conductivity (TRMC) measurements were performed in a cavity cell using a frequency-tripled Q-switched Nd:YAG laser at a wavelength of

355 nm as the excitation source with a 7 ns pulse. Microwaves in the X-band region (8.4–8.7 GHz) were generated by a voltage controlled oscillator (SiversIMA VO3262X). Further details of the TRMC measurement have been described elsewhere.³²⁻³⁵

Photoelectrochemical measurements were performed in a three-electrode configuration under the control of a potentiostat (EG&G PAR 273A). Samples were connected as the working electrode while a Pt wire was used as the counter electrode (total area is 7-8 times larger than that of the working electrode), and Ag/AgCl electrode (XR300, saturated KCl/AgCl solution, Radiometer Analytical) as the reference electrode. For current-voltage curve measurements, samples were tested in 0.1 M potassium phosphate buffer (KPi, pH = 7) electrolyte at a scan rate of 25 mV s⁻¹. The photocurrent was measured under AM1.5 solar illumination (100 mW/cm²) with a solar simulator (WACOM, type WXS-50S-5H, class AAA). Incident photon-to-current conversion efficiencies (IPCE) measurements utilized a 300 W xenon lamp (Oriel) connected with a grating monochromator (Acton Spectra Pro 2155). Electrical impedance spectroscopy (EIS) measurements were conducted with a Zahner Elektrik potentiostat (Model IM6).

Results and discussion

Spray-deposited FeVO₄ photoanodes

Fig. 1a shows the X-ray diffraction (XRD) pattern of both the as-deposited and annealed films. Although the triclinic crystal structure of FeVO₄ already emerges in as-deposited films, annealing at 650 °C for 2 minutes results in higher crystallinity. All peaks match the standard reported pattern for FeVO₄, except for one peak of Fe₂V₄O₁₃ (2θ = 12.56°), which only appears after the high temperature annealing. The molar ratio of secondary phase Fe₂V₄O₁₃ is calculated to be 4.4 % from the Rietveld refinement of the XRD pattern. No hematite (α-Fe₂O₃) peaks are present. This is also found to be the case for various thicknesses of the film (from 25 to 800 nm), as shown in **Fig. S1**. We note that the presence of the secondary phase was only found in films deposited on FTO; no secondary phase was detected for films deposited on quartz (**Fig. S2**).

Scanning electron micrographs show that the as-deposited films have the morphology of stacked rough particles (**Fig. S3**). Upon annealing, they become interconnected grains with a size of 100-400 nm (**Fig. 1b**). The smooth grain surface is in agreement with the higher crystallinity shown by the XRD data. Cross-section SEM images (**Fig. S4**) show films with a homogeneous thickness, similar to other materials prepared by spray pyrolysis in the same spray setup.^{31,34} Based on the cross-section of samples sprayed with 50 mL and 100 mL of precursor, we obtained thickness values of ~200 nm and ~400 nm respectively (**Fig. S4a, b**), indicating a linear relationship between the precursor volume and film thickness.

The absorption spectrum of a 200 nm FeVO₄ film is shown in **Fig. 2a**, as obtained from UV-vis spectroscopy using an integrating sphere configuration (spectra for other thicknesses are shown in **Fig. S5**). The presence of the secondary phase does not affect the overall absorption spectrum, since spectra for

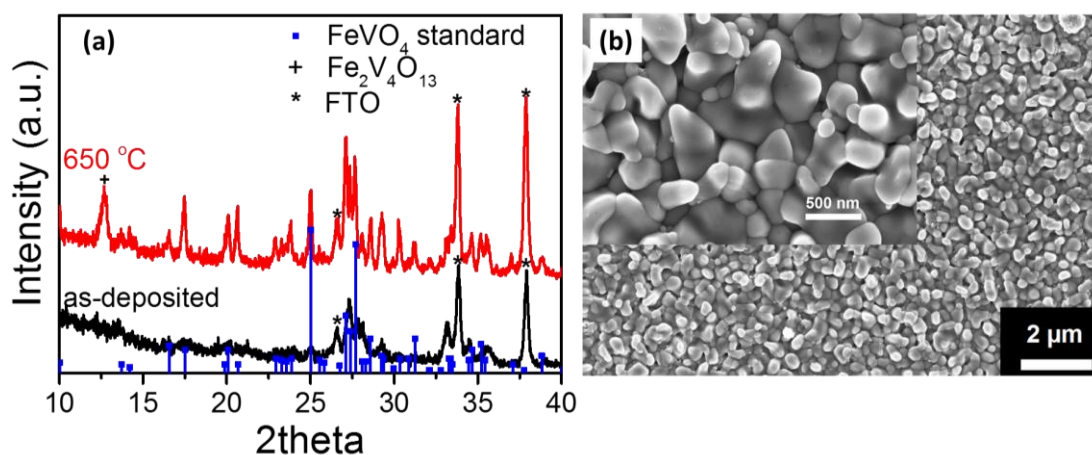


Fig. 1 (a) XRD pattern of as-deposited (black) and annealed (red) films. The reference pattern for FeVO_4 is shown in blue. FTO and $\text{Fe}_2\text{V}_4\text{O}_{13}$ peaks are also labeled. (b) SEM image of FeVO_4 film annealed at 650 °C for 2 minutes in air. Inset shows the same morphology in smaller magnification.

films deposited on FTO (4.4 mol% of $\text{Fe}_2\text{V}_4\text{O}_{13}$ secondary phase is present) and films deposited on quartz (no secondary phase) do not show any significant difference (Fig. S6). The absorption edge is ~ 600 nm, and the films appear yellow/orange in color (Fig. S7). The absorption coefficient (α) can be calculated by the following equation:

$$\alpha = \frac{-\ln(1 - A)}{d} \quad (1)$$

where A is the absorption at a single wavelength and d the film thickness. Fig. 2b shows α as a function of photon energy (wavelength), as obtained from the 200 nm film. For photons with energy above 2.6 eV (wavelength 480 nm), the absorption coefficient calculated is between 4×10^4 and 10^5 cm^{-1} ,

corresponding to a penetration depth (α^{-1}) of ~ 100 –250 nm. Overall, a thickness of 400 nm is needed to absorb $\sim 60\%$ of all AM1.5 photons with wavelengths above the bandgap of FeVO_4 . The calculated Tauc plots (Fig. 2c) demonstrate that FeVO_4 has a direct band gap of ~ 2.6 eV and an indirect band gap of ~ 2.07 eV, enabling a wide range of visible light absorption. The indirect band gap of 2.07 eV agrees with reported values in the literature.^{27, 28}

The photocurrents of samples with various thicknesses are shown in Fig. 3a. The current-voltage (J-V) curve of FeVO_4 films under chopped simulated solar light shows moderate photocurrent but a relatively high onset potential of ~ 0.68 V vs. RHE (Fig. S8). This is in excellent agreement with the flatband potential of the film, which is $\sim 0.69 \pm 0.06$ V vs. RHE, according

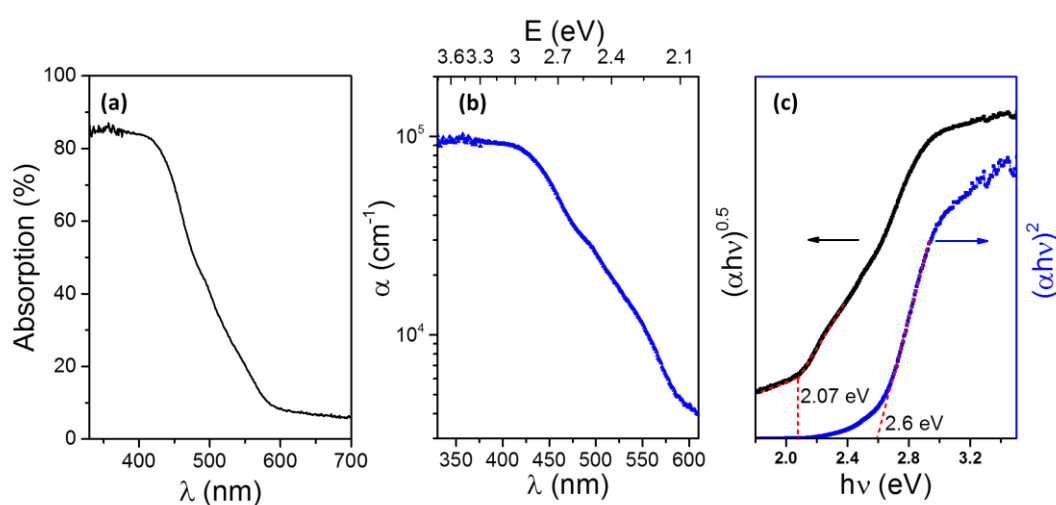


Fig. 2 (a) Absorption spectrum, (b) calculated absorption coefficient (α), plotted as a function of photon energy and wavelength, and (c) Tauc plot of 200 nm FeVO_4 film annealed at 650 °C.

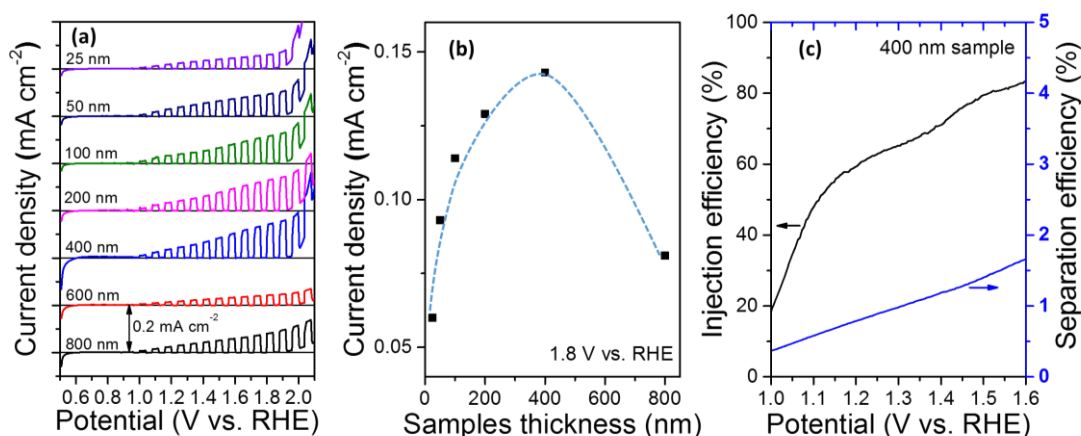


Fig. 3 (a) Current-voltage curves of samples from 25 nm to 800 nm measured in 0.1 M KPI (pH = 7) under chopped AM1.5 illumination. (b) The photocurrent at 1.2 V vs. RHE as a function of the film thickness. Dashed blue line is a guide to the eye. (c) Charge separation and injection efficiency of the 400 nm FeVO₄ sample.

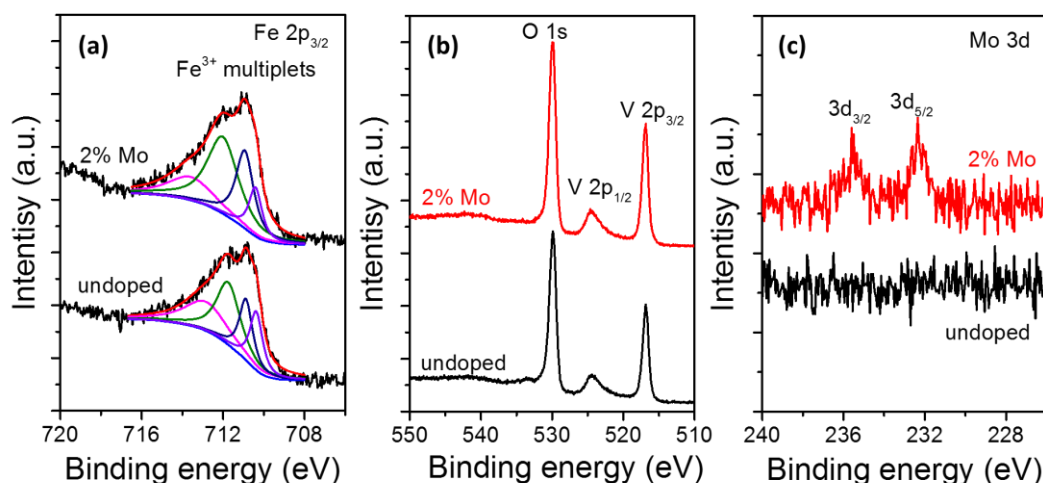


Fig. 4 Core level XPS spectra of (a) Fe, (b) O and V, and (c) Mo of undoped and 2% Mo doped samples.

to the Mott-Schottky analysis (Fig. S9). UPS measurements (Fig. S10) reveal a work function value of 5.1 ± 0.15 eV (i.e., the Fermi level is ~ 0.6 V vs. RHE), which corresponds well with the onset potential and the flatband potential. The optimum thickness is found to be 400 nm, as shown in Fig. 3b; this is presumably caused by the competition between absorption depth and diffusion length of the photogenerated carriers in FeVO₄.

The photocurrent obtained (0.15 mA cm^{-2}) is comparable to previously reported values,²⁸ but it is still lower than the theoretical photocurrent based on the band gap (13 mA cm^{-2}). In order to understand the cause for such a low photocurrent, further photoelectrochemical measurements were carried out in electrolyte containing Na₂SO₃ as hole scavenger to distinguish the bulk charge separation from surface charge injection efficiencies (see Supporting Information on calculation steps). The calculated η_{sep} and η_{inj} of the 400 nm-thick sample are shown in Fig. 3c. η_{inj} increases with applied potential and

reaches a value of 60–80% at potentials above 1.2 V vs. RHE. On the other hand, η_{sep} remains lower than 2% over the potential range. We note that this may be partially contributed to the presence of the secondary phase, which affects the photocurrent negatively. Nevertheless, this analysis suggests that the surface charge injection in FeVO₄ is not the main problem, but the bulk carrier separation is.

Mo doping of FeVO₄

One common method to address the problem of poor charge separation in the bulk is to improve the conductivity by doping.^{11, 36–38} Here, we introduced Mo to the 200 nm-thick FeVO₄ films (200 nm was chosen as the thickness here since there is only minute differences of photocurrent with the 400 nm, but with much faster deposition time), by simply adding a Mo precursor into the spray deposition solution as mentioned in the experimental section. Mo⁶⁺ is expected to replace V⁵⁺

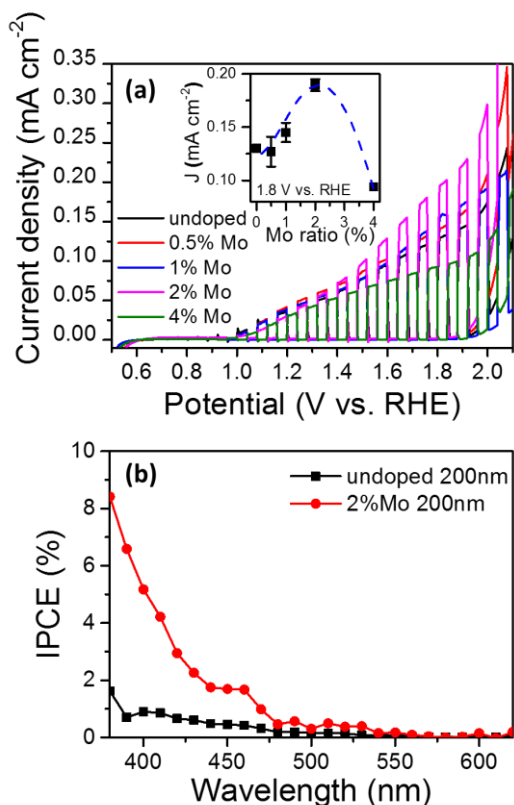
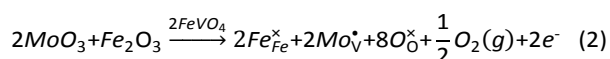


Fig. 5 (a) J-V curves of undoped and doped samples measured in 0.1 M KPi (pH = 7). Inset shows the current density changes with Mo doping ratio. (b) IPCE of 2% Mo doped and undoped sample measured at 1.6 V vs. RHE.

according to the following defect-chemical equation (in Kröger-Vink notation):



If no trapping at defects sites occurs, the additional electrons will reside in the conduction band and improve the bulk conductivity of the film. This is confirmed by the 5-fold improvement in carrier concentration upon 2% Mo-doping, based on the Mott-Schottky analysis (Fig. S9). Upon addition of Mo, no additional peaks are observed in XRD patterns (Fig. S11). Although this does not exclude the possibility that small amounts of X-ray amorphous or nanocrystalline Mo-oxide have segregated out, the systematic shift of the FeVO_4 XRD peaks is clear evidence of the successful incorporation of Mo into FeVO_4 lattice (Fig. S12).³⁹ No significant changes in morphology or optical absorption are observed for the Mo-doped films when compared to the undoped ones (Fig. S13-14).

The chemical composition of the films was investigated by XPS. No other elements or contaminants (except adventitious carbon) are detected in the survey spectrum (Fig. S15). The core level spectra are displayed in Fig. 4 to show the oxidation states of elements. Fig. 4a shows the Fe $2p_{3/2}$ peaks located at 709–716 eV, which can be fitted to the Fe^{3+} multiplets, indicating that Fe exhibits a valence state of 3+ in FeVO_4 .^{29, 40} The binding energy

of V is 516.85 eV (Fig. 4b), which represents a V^{5+} oxidation state.^{11, 41} The O 1s peak is located at 529.9 eV, close to the position expected for a surface lattice oxygen peak.¹¹ No significant change is observed in the Fe, V, and O peaks upon Mo introduction. The signal of Mo 3d core level (Fig. 4c) confirms the successful incorporation of Mo in the 2% Mo doped sample. The binding energy of Mo $3d_{5/2}$ at ~ 232.3 eV confirms that Mo exists in the 6+ oxidation state.^{11, 42} The Mo/(Mo+V) atomic ratio is calculated to be $1.9 \pm 0.1\%$ from XPS results, which is in well agreement with the concentration of Mo in the precursor.

The photocurrents under chopped AM1.5 illumination for FeVO_4 with varying Mo concentration are shown in Fig. 5a. The photocurrent increases with increasing Mo concentration and reaches a maximum for 2% Mo concentration (see inset of Fig. 5a); beyond this the photocurrent decreases. For the 2% Mo doped film, we obtained a photocurrent improvement of $\sim 40\%$ at potentials higher than 1.6 V vs. RHE, as compared to the undoped film. Again, we carefully note that the photocurrent may be affected (either positively or negatively) by the presence of the $\text{Fe}_2\text{V}_4\text{O}_{13}$ secondary phase. Overall, our photocurrent is

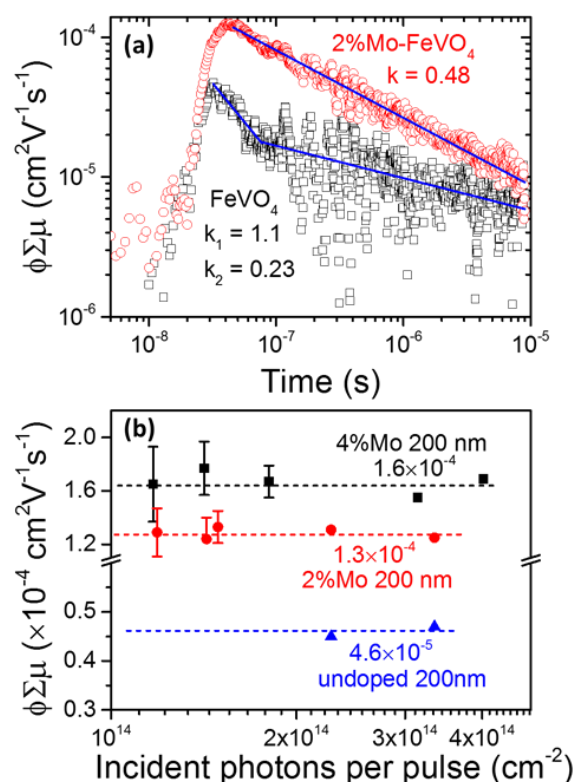


Fig. 6 (a) Time-resolved microwave conductivity (TRMC) signal of 200 nm-thick 2% Mo doped and undoped FeVO_4 films excited by 355 nm laser with an intensity of 3.35×10^{14} photons pulse⁻¹ cm⁻². The blue solid lines are the power law fits of the curves. k , k_1 and k_2 are the decay exponents. (b) Calculated mobility for 2%, 4% Mo doped samples and undoped samples from different light intensities.

comparable with other reports on FeVO_4 in the literature, as summarized in **Table S1**.

The IPCE of the undoped and 2% Mo films are shown in **Fig. 5b**. Consistent with the AM1.5 photocurrent results, the 2% Mo doped sample shows a strongly enhanced efficiency between 380–480 nm. At longer wavelengths, the IPCE is also improved, but remains lower than 1%. The 480 nm wavelength corresponds to a photon energy of 2.6 eV, which is exactly the direct band gap of FeVO_4 (**Fig. 2**). Thus, it appears that the direct optical transition contributes much more to the total photocurrent than the indirect one. The charge separation and injection efficiencies of the 2% Mo doped sample were also measured to investigate the influence of doping (**Fig. S16**). Interestingly, η_{inj} improves with doping, with values over 90% at potentials larger than 1.35 V vs. RHE. η_{sep} also improves upon Mo doping, but the values remain very low (< 3%).

In order to understand the reason for the very low carrier separation efficiency—even after Mo doping—we performed time-resolved microwave conductivity (TRMC) to investigate the carrier transport properties (i.e., mobility, lifetime, diffusion length) of FeVO_4 . Only a moderate amplitude of TRMC signals is detected from the undoped FeVO_4 film (**Fig. 6a**). The TRMC signal ($\phi\Sigma\mu$) of the undoped sample decays rapidly within the

first 100 ns, after which it becomes very noisy. The decay curve of the undoped sample can be fitted with power law ($\phi\Sigma\mu = 0.0012 \times t^{-1.06}$, $t < 100$ ns) and the mobility is estimated to be $\sim 4.6 \times 10^{-5} \text{ cm}^2 \text{ V}^{-1} \text{ s}^{-1}$. Upon Mo doping, the microwave signal significantly increases and a clear prolonged decay is observed (**Fig. 6a**). The decay curve fits well with power law ($\phi\Sigma\mu = 2.66 \times t^{-0.48}$) over a time window ranging from ns to 10 μs (see **Fig. 6a**). Mobility values of $1.3 \times 10^{-4} \text{ cm}^2 \text{ V}^{-1} \text{ s}^{-1}$ and $1.6 \times 10^{-4} \text{ cm}^2 \text{ V}^{-1} \text{ s}^{-1}$ are extrapolated for AM 1.5 conditions ($\sim 10^9$ photons pulse $^{-1}$ cm $^{-2}$) for 2% and 4% Mo doped samples, respectively (**Fig. 6b**). These values are ~ 3 times larger than that of the undoped sample.

The power law decay implies a trap-limited bimolecular recombination mechanism instead of regular band-band recombination.⁴³ Such behavior is consistent with the relatively constant mobility and similar decay kinetics at various light intensities (**Fig. S17**). The decay curves for 2% and 4% Mo-doped samples have the same decay exponent of -0.5. This suggests an identical decay mechanism, most probably due to the interaction (i.e. trapping and detrapping) of charge carriers with a wide distribution of states in the band gap (multiple trapping).⁴⁴ The undoped sample, however, decays much faster than the doped ones in the first ~ 100 ns, where the decay exponent is close to -1.

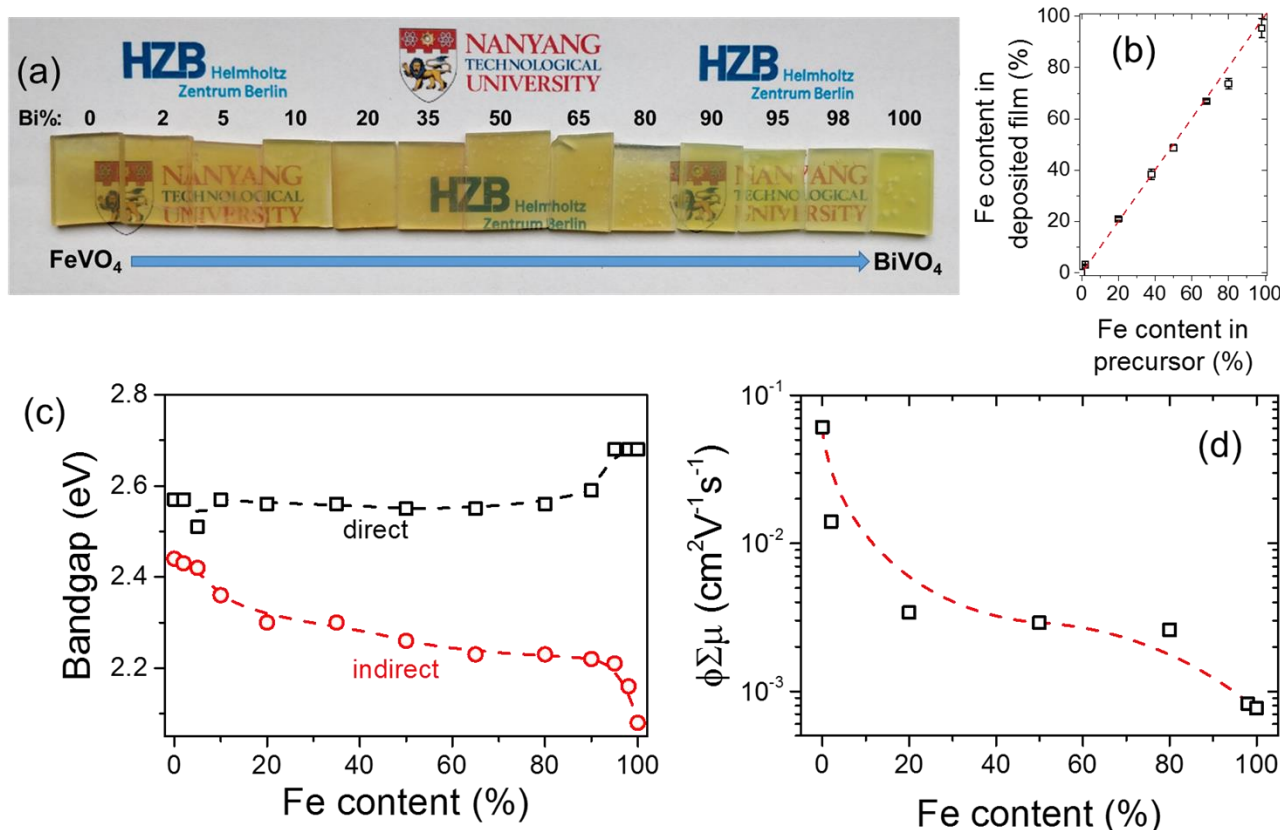


Fig. 7 (a) Photographs of films with various Fe content, from BiVO_4 (far left) to FeVO_4 (far right). (b) Correlation between Fe content added in the precursor to the Fe content in the deposited films measured by EDX. (c) Band gap (direct and indirect) values of films as a function of Fe content. Values are taken from the Tauc plots. (d) TRMC-obtained mobility as a function of Fe content in the film.

The power law decay has been empirically ascribed to trapping-detrapping or carrier tunneling models.^{43, 45-47} For the trapping-detrapping model, a distribution of trap states that leads to a distribution of trapping-detrapping times results in a broad range of recombination time constants and a decay exponent between 0 and -1.⁴⁶ Alternatively, in the carrier tunneling model, the trapped carriers can tunnel to adjacent recombination sites; the broad range of tunneling time constants is then a result of a distribution of short distances between the trap states and the recombination centers. The possibility of tunneling for the undoped samples is inferred from the power law exponent (~ -1), which indicates zero-order kinetics, and recombination centers that are close to each other (within a few nm). The addition of Mo leads to a slower decay with a power law exponent of -0.5, which suggests that Mo could prevent fast tunneling, possibly by the interaction of Mo excess electrons with trap states (i.e., pre-filling). The exact mechanism for our data is unknown and beyond the scope of this work; further experiments are needed to discriminate this.

The lifetime of the charge carriers, τ , is defined as the time that it takes for the signal to decrease to 50% of its starting value. Values of 29 and 136 ns are found for undoped and 2% Mo doped samples, respectively. Based on these lifetimes and mobilities, the diffusion lengths were calculated to be ~ 2 nm for undoped and ~ 7 nm for 2% Mo doped FeVO₄. The improvement in the carrier transport properties for Mo-doped FeVO₄ is consistent with the photocurrent improvement obtained upon Mo-doping. Nevertheless, the values are relatively low, even with Mo-doping, which explains the very low carrier separation efficiency.

Mixed phase FeVO₄-BiVO₄

The sections above revealed that although FeVO₄ has an extended optical absorption as compared to BiVO₄, the carrier mobility is 2-3 orders of magnitude lower. To overcome this trade-off, we investigated the possibility of maintaining the carrier mobility while extending the visible light absorption by partial substitution of cation Fe³⁺ with Bi³⁺ in FeVO₄. Therefore, a series of samples with different Fe ratios were fabricated under same conditions by mixing Fe and Bi precursors in different Fe/Bi molar ratio ((Fe+Bi)/V = 1:1). The samples are denoted as Fe_{1-x}Bi_xVO₄ (0 \leq x \leq 1, e.g., Fe_{0.2}Bi_{0.8}VO₄) (Supplementary note 3).

Films with different Fe ratios demonstrated a gradual color change from brownish orange (100% Fe, FeVO₄) to bright yellow (0 % Fe, BiVO₄) (Fig. 7a). Energy-dispersive X-ray (EDX) spectroscopy shows the Fe/Bi ratio matches well with that in precursor (Fig. 7b). XRD patterns show a gradual change from monoclinic BiVO₄ to triclinic FeVO₄ with increasing Fe content (Fig. S19). However, the peak intensity of FeVO₄ is relatively low, due to the use of moderate annealing temperature of 450 °C (instead of the 650 °C that causes high crystallinity of FeVO₄). Annealing above 450 °C was found to cause vanadium loss in BiVO₄. Therefore, higher annealing temperatures were avoided.

Increasing Fe/Bi ratio in the film leads to the extension of absorption spectra obtained from UV-vis measurements (Fig. S20). For films with an Fe content higher than 5%, a substantial

improvement of absorption in the range of 500–600 nm was observed, which is beyond the absorption onset of pure BiVO₄ (~ 500 nm). Fig. 7c illustrates the influence of Fe content to the apparent band gap values of the films. With increasing Fe content, the direct band gap is relatively constant at ~ 2.6 eV, but the effective indirect band gap decreases from 2.4 to 2.1 eV. At the same time, TRMC-derived mobility of the films decreases with increasing Fe content (Fig. 7d). These suggest that an optimum concentration of Fe might exist, in which the loss in mobility is compensated by the increased optical absorption. Unfortunately, initial photoelectrochemical measurements do not show additional photocurrent beyond the band gap of BiVO₄, possibly due to the limitation to anneal at higher temperature, which is required to obtain highly crystalline FeVO₄. Alternative deposition techniques (e.g., pulsed laser deposition) that can produce high quality crystalline material without the need of post-deposition annealing should be considered in order to obtain Fe_{1-x}Bi_xVO₄ films with good photoelectrochemical properties.

Conclusions

Spray-deposited n-type triclinic FeVO₄ films have been systematically assessed as a candidate photoanode material. The band gap is 2.07 eV as obtained from optical measurements, which is close to the ideal band gap range for a light absorber (1.7–1.9 eV). Time-resolved microwave conductivity measurements reveal that the low carrier mobility of FeVO₄ is the main factor that limits its PEC performance (see Table S2 for comparison with other metal oxides). The low mobility results in poor conductivity and very limited carrier diffusion lengths. As a result, the photogenerated charge carriers are primarily lost through bulk recombination, resulting in a very low separation efficiency of $\sim 1\%$. Doping is partially effective in improving the photocurrent, as also shown in other reports.^{28, 30} In our case, Mo-doping leads to significant enhancement in carrier mobility ($\times 3$) and lifetime ($\times 4.5$), which results in 45% increase of the photocurrent density at 1.6 V vs. RHE and major enhancement of the IPCE (7% at 400 nm, vs. 1% for the undoped film). Nevertheless, the carrier diffusion lengths for the doped films are still less than 10 nm; further efforts in improving the carrier separation efficiency (e.g., nanostructuring, heterojunction formation) need to be pursued. In addition, the high donor densities even in the undoped films may also suggest the presence of high amount of intrinsic defects generated during the synthesis process, which can act as recombination centers. Higher quality films deposited with greater control over defects (e.g., pulsed laser deposition) need to be developed in order to further improve the PEC performance of FeVO₄. Finally, we have proposed a mixed phase iron bismuth vanadate compound (Fe_{1-x}Bi_xVO₄) in order to enhance the charge carrier mobility. While the mobility indeed improves with increasing Bi content, the optical absorption edge shifts towards higher energies; a delicate balance between this trade-off may potentially result in an optimum photoelectrode. The materials parameters and

insights from this study are expected to help the further development of FeVO₄ and related photoelectrodes.

Conflicts of interest

There are no conflicts to declare.

Acknowledgements

We acknowledge Christian Höhn and Paul Plate for performing the XPS and UPS measurements as well as Fanxing Xi for the assistance with SEM measurements. Mengyuan Zhang thanks the support of Nanyang Technological University (NTU) Research Scholarship and Deutscher Akademischer Austauschdienst (DAAD) research grant (#57214225) for the research stay at Helmholtz-Zentrum Berlin. Financial support from the Singapore Ministry of Education (MOE) Tier 2 grant no MOE2016T21030 and Singapore-German Mobility 2014 are gratefully acknowledged.

References

1. Y. Park, K. J. McDonald and K.-S. Choi, *Chem. Soc. Rev.*, 2013, **42**, 2321-2337.
2. K. Sivula and R. van de Krol, *Nat. Rev. Mater.*, 2016, **1**, 15010.
3. F. F. Abdi and S. P. Berglund, *J. Phys. D, Appl. Phys.*, 2017, **50**, 193002.
4. T. W. Kim and K.-S. Choi, *Science*, 2014, **343**, 990-994.
5. J. A. Seabold and K.-S. Choi, *J. Am. Chem. Soc.*, 2012, **134**, 2186-2192.
6. F. F. Abdi, N. Firet and R. van de Krol, *ChemCatChem*, 2013, **5**, 490-496.
7. F. F. Abdi, L. Han, A. H. M. Smets, M. Zeman, B. Dam and R. van de Krol, *Nat. Commun.*, 2013, **4**.
8. J. A. Seabold, K. Zhu and N. R. Neale, *Phys. Chem. Chem. Phys.*, 2014, **16**, 1121-1131.
9. W. J. Jo, J.-W. Jang, K.-j. Kong, H. J. Kang, J. Y. Kim, H. Jun, K. P. S. Parmar and J. S. Lee, *Angew. Chem. Int. Ed.*, 2012, **51**, 3147-3151.
10. K. P. S. Parmar, H. J. Kang, A. Bist, P. Dua, J. S. Jang and J. S. Lee, *ChemSusChem*, 2012, **5**, 1926-1934.
11. R. P. Antony, P. S. Bassi, F. F. Abdi, S. Y. Chiam, Y. Ren, J. Barber, J. S. C. Loo and L. H. Wong, *Electrochim. Acta*, 2016, **211**, 173-182.
12. J. Su, L. Guo, N. Bao and C. A. Grimes, *Nano Lett.*, 2011, **11**, 1928-1933.
13. Z.-F. Huang, L. Pan, J.-J. Zou, X. Zhang and L. Wang, *Nanoscale*, 2014, **6**, 14044-14063.
14. P. M. Rao, L. Cai, C. Liu, I. S. Cho, C. H. Lee, J. M. Weisse, P. Yang and X. Zheng, *Nano Lett.*, 2014, **14**, 1099-1105.
15. Y. Pihosh, I. Turkevych, K. Mawatari, J. Uemura, Y. Kazoe, S. Kosar, K. Makita, T. Sugaya, T. Matsui, D. Fujita, M. Tosa, M. Kondo and T. Kitamori, *Sci. Rep.*, 2015, **5**, 11141.
16. J. K. Cooper, S. Gul, F. M. Toma, L. Chen, Y.-S. Liu, J. Guo, J. W. Ager, J. Yano and I. D. Sharp, *J. Phys. Chem. C*, 2015, **119**, 2969-2974.
17. L. C. Seitz, Z. Chen, A. J. Forman, B. A. Pinaud, J. D. Benck and T. F. Jaramillo, *ChemSusChem*, 2014, **7**, 1372-1385.
18. S. Hu, C. Xiang, S. Haussener, A. D. Berger and N. S. Lewis, *Energy & Environ. Sci.*, 2013, **6**, 2984-2993.
19. M. S. Prévot and K. Sivula, *J. Phys. Chem. C*, 2013, **117**, 17879-17893.
20. B. Seger, O. Hansen and P. C. K. Vesborg, *Solar RRL*, 2017, **1**, e201600013.
21. S. Hu, M. R. Shaner, J. A. Beardslee, M. Lichterman, B. S. Brunschwig and N. S. Lewis, *Science*, 2014, **344**, 1005-1009.
22. J. D. Benck, S. C. Lee, K. D. Fong, J. Kibsgaard, R. Sinclair and T. F. Jaramillo, *Adv. Energy Mater.*, 2014, **4**, 1400739.
23. J. R. McKone, A. P. Pieterick, H. B. Gray and N. S. Lewis, *J. Am. Chem. Soc.*, 2013, **135**, 223-231.
24. M. H. Lee, K. Takei, J. Zhang, R. Kapadia, M. Zheng, Y.-Z. Chen, J. Nah, T. S. Matthews, Y.-L. Chueh, J. W. Ager and A. Javey, *Angew. Chem. Int. Ed.*, 2012, **51**, 10760-10764.
25. S. Gupta, Y. P. Yadava and R. A. Singh, *J. Mater. Sci. Lett.*, 1986, **5**, 736-738.
26. T. Arai, Y. Konishi, Y. Iwasaki, H. Sugihara and K. Sayama, *J. Comb. Chem.*, 2007, **9**, 574-581.
27. C. D. Morton, I. J. Slipper, M. J. K. Thomas and B. D. Alexander, *J. Photochem. and Photobiol., A*, 2010, **216**, 209-214.
28. S. K. Biswas and J.-O. Baeg, *Int. J. Hydrogen Energy*, 2013, **38**, 14451-14457.
29. M. Balamurugan, G. Yun, K.-S. Ahn and S. H. Kang, *J. Phys. Chem. C*, 2017, **121**, 7625-7634.
30. W. Wang, Y. Zhang, L. Wang and Y. Bi, *J. Mater. Chem. A*, 2017, **5**, 2478-2482.
31. F. F. Abdi, N. Firet, A. Dabirian and R. van de Krol, *MRS Proc.*, 2012, **1446**.
32. F. F. Abdi, T. J. Savenije, M. M. May, B. Dam and R. van de Krol, *J. Phys. Chem. Lett.*, 2013, **4**, 2752-2757.
33. M. S. Prévot, X. A. Jeanbourquin, W. S. Bourée, F. Abdi, D. Friedrich, R. van de Krol, N. Guijarro, F. Le Formal and K. Sivula, *Chem. Mater.*, 2017, **29**, 4952-4962.
34. F. F. Abdi, A. Chemseddine, S. P. Berglund and R. van de Krol, *J. Phys. Chem. C*, 2017, **121**, 153-160.
35. M. Ziwrtsch, S. Müller, H. Hempel, T. Unold, F. F. Abdi, R. van de Krol, D. Friedrich and R. Eichberger, *ACS Energy Lett.*, 2016, **1**, 888-894.
36. B. Iandolo, B. Wickman, I. Zoric and A. Hellman, *J. Mater. Chem. A*, 2015, **3**, 16896-16912.
37. Gurudayal, S. Y. Chiam, M. H. Kumar, P. S. Bassi, H. L. Seng, J. Barber and L. H. Wong, *ACS Appl. Mater. Interfaces*, 2014, **6**, 5852-5859.
38. P. S. Bassi, Gurudayal, L. H. Wong and J. Barber, *Phys. Chem. Chem. Phys.*, 2014, **16**, 11834-11842.
39. H. S. Park, K. E. Kweon, H. Ye, E. Paek, G. S. Hwang and A. J. Bard, *J. Phys. Chem. C*, 2011, **115**, 17870-17879.
40. A. P. Grosvenor, B. A. Kobe, M. C. Biesinger and N. S. McIntyre, *Surf. Interface Anal.*, 2004, **36**, 1564-1574.
41. Y. Liu, Y. Guo, L. T. Schelhas, M. Li and J. W. Ager, *J. Phys. Chem. C*, 2016, **120**, 23449-23457.
42. W. Yao, H. Iwai and J. Ye, *Dalton Trans.*, 2008, **0**, 1426-1430.
43. J. Ravensbergen, F. F. Abdi, J. H. van Santen, R. N. Frese, B. Dam, R. van de Krol and J. T. M. Kennis, *J. Phys. Chem. C*, 2014, **118**, 27793-27800.
44. D. Friedrich and M. Kunst, *Nano Energy*, 2012, **1**, 303-308.
45. M. Kuno, D. P. Fromm, H. F. Hamann, A. Gallagher and D. J. Nesbitt, *J. Chem. Phys.*, 2000, **112**, 3117-3120.

46. J. Nelson and R. E. Chandler, *Coord. Chem. Rev.*, 2004, **248**, 1181-1194.
47. P. H. Sher, J. M. Smith, P. A. Dalgarno, R. J. Warburton, X. Chen, P. J. Dobson, S. M. Daniels, N. L. Pickett and P. O'Brien, *Appl. Phys. Lett.*, 2008, **92**, 101111.